Retrieval of $O_2(^1\Sigma)$ and $O_2(^1\Delta)$ volume emission rates in the mesosphere and lower thermosphere using SCIAMACHY MLT limb scans

Amirmahdi Zarboo[1], Stefan Bender[1], John P. Burrows[2], Johannes Orphal[1], and Miriam Sinnhuber[1]

[1]Karlsruhe Institute of Technology, Germany
[2]University of Bremen, Germany

Correspondence to: Amirmahdi Zarboo (amirmahdi.zarboo@kit.edu)

Abstract. We present the retrieved volume emission rates (VER) from the airglow of both the daytime and twilight $O_2(^1\Sigma)$ band and $O_2(^1\Delta)$ band emissions in the mesosphere/lower thermosphere (MLT). The SCanning Imaging Absorption spectroMeter for Atmospheric CHartographY (SCIAMACHY) on-board the European Space Agency Envisat satellite observes upwelling radiances in limb viewing geometry during its special MLT mode over the range 50 to 150 km. In this study we use
5 the limb observations in the visible (595–811 nm) and near infrared (1200–1360 nm) bands.

We have investigated the daily mean latitudinal distributions and the time series of the retrieved VER in the altitude range from 53 to 149 km. The maximal observed VER of $O_2(^1\Delta)$ during daytime are typically 1 to 2 orders of magnitude larger than those of $O_2(^1\Sigma)$. The latter peaks at around 90 km, whereas the $O_2(^1\Delta)$ emissivity decreases with altitude, with the largest values at the lower edge of the observations (about 53 km). The VER values in the upper mesosphere (above 80 km) are found
10 to depend on the position of the sun, with pronounced high values occurring during summer for $O_2(^1\Delta)$. $O_2(^1\Sigma)$ emissions show additional high values at polar latitudes during winter and spring. These additional high values are presumably related to the downwelling of atomic oxygen after large sudden stratospheric warmings (SSW). Accurate measurements of the $O_2(^1\Sigma)$ and $O_2(^1\Delta)$ airglow, provided that the mechanism of their production is understood, yield valuable information about both the chemistry and dynamics in the MLT. For example, they can be used to infer the amounts and distribution of ozone, solar
15 heating rates and temperature in the MLT.

1   Introduction

The atmospheric airglow in the mesosphere and thermosphere above ≈ 60 km is formed by fluorescent emission from excited states of atoms and molecules. Atoms and molecules in the mesosphere and lower thermosphere can be excited by absorption of solar radiation (photoluminescence), or by exothermic chemical reactions (chemiluminescence), see, e.g., Brasseur and
20 Solomon (2006).

The processes that contribute to the airglow of atomic and molecular oxygen in the mesosphere and lower thermosphere are shown in Figure 1. The recombination of atomic oxygen (Barth, 1964), denoted as reaction (R1) and (k) in Figure 1, produces
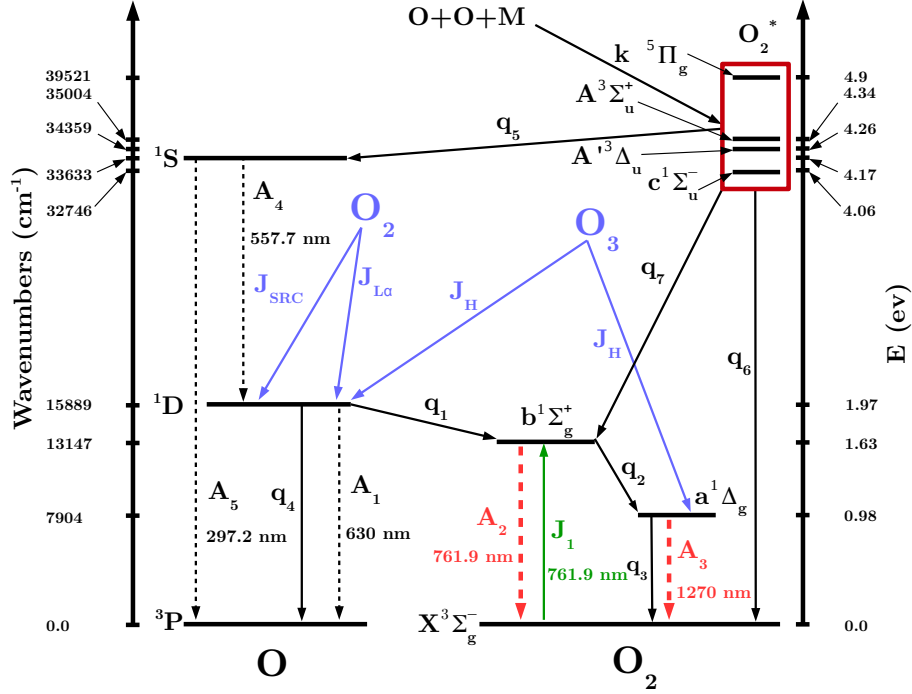
Figure 1. Schematic overview depicting processes that contribute to the production of Oxygen emission bands in the middle atmosphere. The black solid arrows are the most important gas phase reactions (k) and quenching reactions (q_i). The blue and green solid arrows are photo-dissociation and photo-excitation processes respectively (J_i). Dashed arrows correspond to spontaneous radiative emissions (A_i), and the red dashed arrows show the radiative emissions that are the subject of this study. (*) in O_2^* denotes several excited states, see text for explanation.

O_2^* excited molecules:

$$O(^3P) + O(^3P) + M \longrightarrow O_2^* + M; \tag{R1}$$

O_2^* represents any of the seven states below the first dissociation limit. Bates and others argue that the population distribution between these states can best be approximated statistically, in which the $^5\Pi_g$ state is produced in almost 40% of the collisions (Smith, 1984; Bates, 1992; Wraight, 1982). Most of the O_2^* derived from recombination is found in the $A^3\Sigma_u^+$ state (Slanger and Copeland, 2003), and in a recent review Huestis concludes that all of the recombining atoms pass through the Herzberg states $c^1\Sigma_u^-$, $A'^3\Delta_u$, and $A^3\Sigma_u^+$ (Huestis, 2013). Stegman and Murtagh (1991) provide the quenching parameters resulted from analysing the measurements of the near-ultraviolet portion of the nightglow to fit the synthetic spectra of the Herzberg bands of O_2. These parameters set an upper limit of 10% production efficiency on the generation of $O_2(c^1\Sigma_u^-)$ in the atomic

oxygen association reaction . Admittedly, proper accounting of the correct products of (R1) can be complex. Recent research has investigated this issue, e.g. Kirillov (2012, 2014). Therefore we assume the production of a surrogate "hybrid" state O_2^* in the photochemical model.

The photolysis of ozone (J_H in Figure 1, reaction (R2)) in the Hartley band ($\lambda < 310$ nm) leads to the first electronically excited state of atomic oxygen $O(^1D)$ and molecular oxygen $O_2(a^1\Delta_g)$ (DeMore, 1966):

$$O_3 + h\nu(\lambda \leq 310 \text{ nm}) \rightarrow O(^1D) + O_2(a^1\Delta_g). \tag{R2}$$

The photolysis of molecular oxygen in the Schumann-Runge continuum (J_{SRC} in Figure 1, reaction (R3)) and at Lyman α ($J_{L\alpha}$ in Figure 1, reaction (R4)) leads to electronically excited oxygen atoms $O(^1D)$ (Nicolet, 1971):

$$O_2(X^3\Sigma_g^-) + h\nu(130 \leq \lambda \leq 175 \text{ nm}) \rightarrow O(^3P) + O(^1D), \tag{R3}$$

$$O_2(X^3\Sigma_g^-) + h\nu(\lambda = 121.6 \text{ nm}) \rightarrow O(^3P) + O(^1D). \tag{R4}$$

Quenching (collisional de-excitation) processes are represented by black solid arrows and denoted by (q_i) in Figure 1. The O_2^*, produced by reaction (R1), can be quenched by atomic oxygen to produce $O(^1S)$ via reaction (R5) (q_5 in Figure 1) (Barth and Hildebrandt, 1961) or quenched by molecular oxygen to produce $O_2(b^1\Sigma_g^+)$ via reaction (R6) (q_6 in Figure 1) (Greer et al., 1981):

$$O_2^* + O(^3P) \rightarrow O(^1S) + O_2(X^3\Sigma_g^-), \quad (q_5) \tag{R5}$$

$$O_2^* + O_2(X^3\Sigma_g^-) \rightarrow O_2(b^1\Sigma_g^+) + O_2(X^3\Sigma_g^-). \quad (q_6) \tag{R6}$$
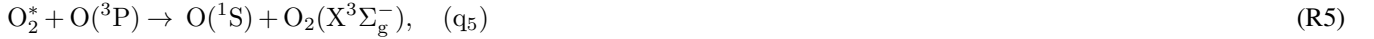
$O(^1D)$ by quenching with $O_2(X^3\Sigma_g^-)$, produces $O_2(b^1\Sigma_g^+)$ via reaction (R7) that combines q_1 and q_4 in Figure 1 (Mlynczak and Olander, 1995):

$$O(^1D) + O_2(X^3\Sigma_g^-) \rightarrow O_2(b^1\Sigma_g^+) + O(^3P). \tag{R7}$$

Photoabsorption of the solar radiation at 761.9 nm produces $O_2(b^1\Sigma_g^+)$ directly via

$$O_2(X^3\Sigma_g^-) + h\nu(\lambda = 761.9 \text{ nm}) \rightarrow O_2(b^1\Sigma_g^+) \tag{R8}$$

in the sunlit mesosphere (Mlynczak et al., 1993), shown in Figure 1 as the radiative excitation J_1.

Then, according to reaction (R9) $O_2(b^1\Sigma_g^+)$ can be reduced in energy to $O_2(a^1\Delta_g)$ by collisions with any of the abundant species such as O_2, N_2, CO_2, O etc. (denoted by "M"), shown as q_2 in Figure 1 (Mlynczak and Olander, 1995):

$$O_2(b^1\Sigma_g^+) + M \rightarrow O_2(a^1\Delta_g) + M. \tag{R9}$$

Note that the above is a fast process (spin-conserved).

$O_2(a^1\Delta_g)$ can in turn be quenched via (R10) (q_3 in Figure 1) to produce $O_2(X^3\Sigma_g^-)$:

$$O_2(a^1\Delta_g) + M \rightarrow O_2(X^3\Sigma_g^-) + M, \tag{R10}$$

which is a slow process (spin forbidden because the ground state is $O_2(X^3\Sigma_g^-)$).

5   Spontaneous radiative emissions are represented by dashed arrows and denoted by (A_i) in Figure 1. $O(^1S)$ decays to $O(^1D)$ by emitting 557.7 nm photons (the oxygen green line, reactions (R11), A_4 in Figure 1), which is fast (because it conserves the spin) (Barth and Hildebrandt, 1961):

$$O(^1S) \rightarrow O(^1D) + h\nu(\lambda=557.7 \text{ nm}). \tag{R11}$$

Reactions (R1), (R5) and (R11) are commonly referred to as the Barth mechanism (Barth and Hildebrandt (1961); see, e.g.,
10 the review by Bates (1981)). The green line emission allows to deduce the atomic oxygen densities near 100 km, as shown for example by Lednyts'kyy et al. (2015). The oxygen 297.2 nm line is one of the prominent components of the ultraviolet nightglow (Slanger et al., 2006), and it is produced by $O(^1S)$ via reaction (R12) (Khomich et al., 2008):

$$O(^1S) \rightarrow O(^3P) + h\nu(\lambda=297.2\,\text{nm}), \tag{R12}$$

indicated by A_5 in Figure 1.

15    $O(^1D)$, produced from ((R2), J_H), ((R3), J_{SRC}), ((R4), J_α), or ((R11), A_4), can be deactivated to the ground state $O(^3P)$ by the slow (spin forbidden) emission:

$$O(^1D) \rightarrow O(^3P) + h\nu(\lambda=630.0\,\text{nm}), \tag{R13}$$

the 630.0 nm red line (Khomich et al., 2008) which is represented by A_1 in Figure 1.

Among the strongest features of the day and night airglow are the infrared atmospheric band ($a^1\Delta_g \rightarrow X^3\Sigma_g^-$) and the
20 atmospheric band ($b^1\Sigma_g^+ \rightarrow X^3\Sigma_g^-$) of molecular oxygen (Wayne, 1994). These two spontaneous radiative emissions, which we deal with in this work, are represented by the thick red dashed arrows in Figure 1. They are emitted by the deactivation of the two excited states of the molecular oxygen $O_2(b^1\Sigma_g^+)$ at 761.9 nm via reaction (R14) (A_2 in Figure 1) and $O_2(a^1\Delta_g)$ at 1.27 μm via reaction (R15) (A_3 in Figure 1) (Mlynczak et al., 1993):

$$O_2(b^1\Sigma_g^+) \rightarrow O_2(X^3\Sigma_g^-) + h\nu(\lambda=761.9 \text{ nm}), \tag{R14}$$

25

$$O_2(a^1\Delta_g) \rightarrow O_2(X^3\Sigma_g^-) + h\nu(\lambda=1.27\ \mu\text{m}). \tag{R15}$$

Assuming that the processes in Figure 1 describe the photochemistry and chemistry, one can deduce ozone densities from measurements of the infrared atmospheric volume emission rates in the $O_2(b^1\Sigma_g^+)$ and $O_2(a^1\Delta_g)$ bands (hereafter $O_2(^1\Sigma)$ and

$O_2(^1\Delta)$ bands, respectively). For this, the rates of all of these processes such as q_1 and q_4 in Figure 1 and in the reactions (R7) and (R9) should be known (e.g., Evans et al. (1968); Thomas et al. (1983); Mlynczak and Olander (1995), Mlynczak et al. (2001)).

1.1   Previous measurements

5 The oxygen airglow was measured from space-borne platforms and rocket experiments in several previous studies. Measurements of the $O_2(^1\Sigma)$ band include the Fabry-Perot interferometer on the Dynamics Explorer 2 (DE-2) satellite (Skinner and Hays, 1985), that were used to study the overall brightness of the emission. The High-resolution Doppler imager (HRDI) on the Upper Atmosphere Research Satellite (UARS) (Hays et al., 1993) measured the Doppler shifts of rotational lines of the $O_2(^1\Sigma)$ atmospheric band to determine the winds in the stratosphere, mesosphere, and lower thermosphere. The Wind Imag-
10 ing Interferometer (WINDII) on the same satellite (Shepherd et al., 1993) measured wind, temperature, and emission rates. The TIMED Doppler Interferometer (TIDI) on the Thermosphere-Ionosphere-Mesosphere Energetics and Dynamics (TIMED) satellite (Killeen et al., 2006) performed remote sensing measurements of upper atmosphere winds and temperatures based on $O_2(^1\Sigma)$ emission. The Remote Atmospheric and Ionospheric Detection System (RAIDS) on the International Space Station's Kibo module (Christensen et al., 2012) measured the limb brightness of the $O_2(^1\Sigma)$ (0,0), (0,1), and (1,1) vibrational band
15 emissions from 80 to 180 km. The Optical Spectrograph and InfraRed Imaging System (OSIRIS), on board the Odin satellite (Sheese et al., 2010), was used to derive temperatures in the mesosphere-lower thermosphere region (MLT) from $O_2(^1\Sigma)$.

Previous measurements of the $O_2(^1\Delta)$ band include observations from the near-infrared spectrometer experiment on the Solar Mesosphere Explorer satellite (SME). SME measured emission from $O_2(^1\Delta)$ produced by photolysis of O_3 (Thomas et al., 1984). The infrared atmospheric band airglow radiometer (IRA) aboard the satellite OHZORA measured the mesospheric
20 ozone profile derived from $O_2(^1\Delta)$ emission (Yamamoto et al., 1988). One part of the Optical Spectrograph and InfraRed Imager System (OSIRIS) instrument on board the Odin satellite is a three channel infrared imager (IRI) that observes the scattered sunlight and the airglow from the oxygen infrared atmospheric band at 1.27 µm (Llewellyn et al., 2004). The TIMED (Thermosphere Ionosphere Mesosphere Energetics and Dynamics)/SABER (Sounding of the Atmosphere using Broadband Emission Radiometry) data were used to measure the $O_2(^1\Delta)$ airglow emission by a channel with central wavelength of
25 1.27µm (Gao et al., 2011a).

All of the above mentioned studies include satellite observations of only one of the O_2 bands, either $O_2(^1\Sigma)$ or $O_2(^1\Delta)$. Simultaneous measurements of both $O_2(^1\Delta)$ and $O_2(^1\Sigma)$ airglow were part of the Mesosphere-Thermosphere Emissions for Ozone Remote Sensing (METEORS) sounding rocket experiment. It was launched from White Sands Missile Range, New Mexico (Mlynczak et al., 2001) and was used to derive ozone concentrations separately from each of the O_2 bands.

30   1.2   Present work

In this work, we retrieve volume emission rates (VERs) from the airglow of the $O_2(^1\Sigma)$ and $O_2(^1\Delta)$ bands in the mesosphere/lower thermosphere (MLT) from the SCanning Imaging Absorption spectroMeter for Atmospheric CHartographY (SCIAMACHY Burrows et al. (1995), Bovensmann et al. (1999) and references therein) on board the European Space Agency

Envisat satellite. We present the retrieval algorithm and $O_2(^1\Sigma)$ and $O_2(^1\Delta)$ band volume emission rates. We analyze daily mean latitudinal distributions of VERs in the altitude range of approximately 50-150 km.

In section 2 we describe the SCIAMACHY dataset and our method to retrieve both the $O_2(^1\Delta)$ and the $O_2(^1\Sigma)$ volume emission rates. Results are presented in section 3, including the retrieved volume emission rates and first results on the temporal and spatial variations of the volume emission rates. We also include one example study of the relation between the temporal variations and the sudden stratospheric warming in 2009. In section 4 we summarize the findings of our study and give conclusions.

2 Data and Methods

2.1 Data

The SCanning Imaging Absorption spectroMeter for Atmospheric CHartographY (SCIAMACHY) is a passive remote sensing spectrometer that observes back scattered, reflected, transmitted, or emitted radiation from the atmosphere and the Earth's surface in the 240-2380 nm wavelength range. The instrument is part of the atmospheric chemistry payload onboard the Envisat satellite, which was operational from March 2002 until April 2012. SCIAMACHY has three different viewing geometries: nadir, limb, and moon-sun occultations. From July 2008 until April 2012, SCIAMACHY observed the mesosphere and lower thermosphere region (MLT, 50–150 km) regularly twice a month. This special MLT limb mode scans the mesosphere and lower thermosphere in 30 limb points from 50 to 150 km altitude with a vertical spacing of about 3 km. These scans were scheduled in place of the nominal mode scans and there were 20 limb scans along one semi-orbit. Overall 84 days of mesosphere and lower thermosphere limb measurements were carried out. In this work, we use the visible and near infrared spectra from channel 4 (595–811 nm) and channel 6 (1200–1360 nm) in the MLT limb viewing geometry to retrieve volume emission rates (VERs) from the airglow of the $O_2(^1\Sigma)$ and $O_2(^1\Delta)$ bands. Use of the additional channels covering the green line or UV is beyond our current work, and we refer to e.g. Lednyts'kyy et al. (2015).

To generate data for our study, we used the SCIAMACHY data set Level 1b version 8.02 and the SCIAMACHY command line tool `SciaL1c`[1] from the SCIAMACHY calibration tools. We selected two windows for each of the two bands: 750–780 nm for the $O_2(^1\Sigma)$ band (759–767 nm) and 1200-1360 nm for the $O_2(^1\Delta)$ band (1255–1285 nm). We subtract the spectrum measured at ≈ 360 km tangent height as a dark spectrum from the measured spectra at all of the other tangent heights. This spectrum contains some residual spectral (read-out) patterns left from the calibration step and subtracting it from other spectra which have almost the same patterns cancels out that. For the $O_2(^1\Delta)$ band, there are two masked points that appear in every scan located around 1262 nm and 1282 nm.

---

[1]https://earth.esa.int/web/guest/software-tools/content/-/article/scial1c-command-line-tool-4073

2.2 Daytime spectra

A typical orbit starts with a limb measurement of the twilit atmosphere, followed by the solar occultation measurement during sunrise over the North Pole and an optimized limb-nadir sequence. (Bovensmann et al., 1999). Our criterion to select daytime observations out of twilight measurements is that we require the tangent point solar zenith angle to be less than or equal to 88 degrees. Using this approach we avoid twilight measurements and all of the measurement points are located on the day-side.

Examples of the daytime calibrated spectra for orbit number 41455, measured on 03/02/2010 at a mean latitude of 17.3°N and a mean longitude of 94.3°E are shown in Figure 2a for the $O_2(^1\Sigma)$ band and in Figure 2b for the $O_2(^1\Delta)$ band.

The spectral region used to observe the daytime $O_2(^1\Sigma)$ spectrum includes a Rayleigh scattering background which perturbs the retrieval. Consequently it is necessary to estimate the Rayleigh scattering and subtract it from to yield the $O_2(^1\Sigma)$ emission spectra. This background scattering is attributed in part to the up-welling radiation, from multiple scattering in the lower atmosphere, and the terrestrial albedo. This results in an absorption signature for $O_2(^1\Sigma)$ (Sheese et al., 2010). To account for the multiple scattering and absorption by from the ground state $O_2(^3\Sigma_g)$ to the $O_2(^1\Sigma)$, a background signal comprising the $O_2(^1\Sigma)$ spectrum at the highest altitude (≈ 148 km) scaled to the ratio of the mean of the out-of-band radiances is subtracted from the limb spectra at each tangent height. We consider the spectra in the 750–759 nm and 767–780 nm as out-of-band.

After this correction, we subtract a linear background from the whole signal in each level. An example of the background subtracted spectrum containing the $O_2(^1\Sigma)$ emission is shown in Figure 2c.

For the $O_2(^1\Delta)$ band, the absorption signature in the spectral background is negligible compared to the daytime $O_2(^1\Sigma)$ band spectra, therefore we only subtract a linear background from the observation. An example for the daytime $O_2(^1\Delta)$ band spectra with background subtracted is shown in Figure 2d.

2.3 Twilight spectra

Because the tangent point solar zenith angle for the sun being below the horizon varies with tangent altitude, we use equation (1) to calculate the horizon angle for each tangent point (R is the radius of the Earth and h is the tangent point height):

$$\alpha_{\text{horizon}} = \frac{\pi}{2} + \cos^{-1}\left(\frac{R}{R+h}\right). \tag{1}$$

As a criterion to select twilight data, we remove every limb scan in which at least one point measurement has a solar zenith angle less than given by equation (1). Based on this, we obtain the $O_2(^1\Sigma)$ and the $O_2(^1\Sigma)$ background subtracted twilight spectra shown in Figures 3a and 3c for the example orbit (41455). For the twilight $O_2(^1\Delta)$ band, we apply the same background subtraction as for daylight. Figure 3b shows the twilight $O_2(^1\Delta)$ spectra, and Figure 3d shows the background-corrected twilight $O_2(^1\Delta)$ spectra for the same example orbit (41455). It is apparent that the background signal is negligible for both of the $O_2(^1\Sigma)$ and $O_2(^1\Delta)$ twilight spectra.
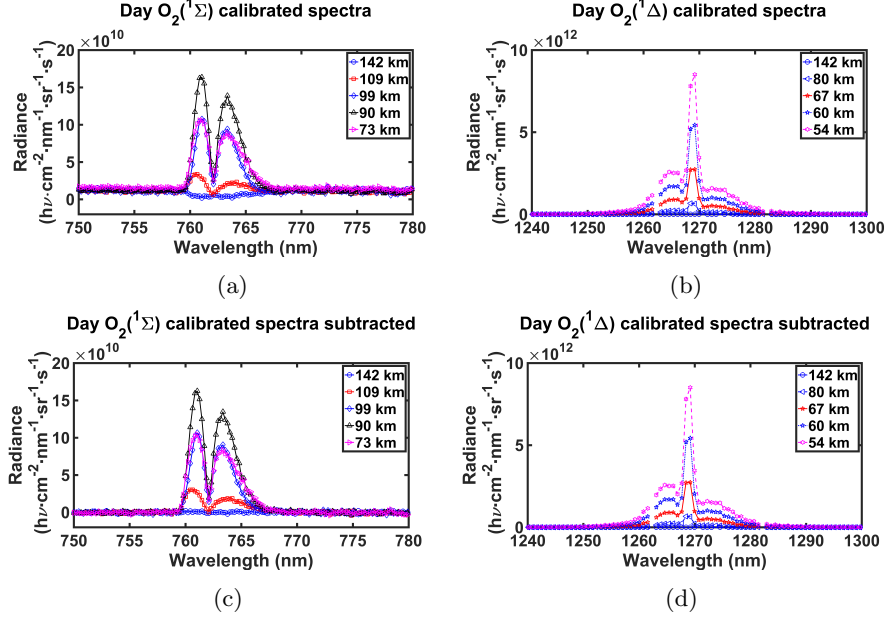
Figure 2. Examples of the daytime calibrated spectra, and the background-corrected spectra. (a) $O_2(^1\Sigma)$ on 03/02/2010, orbit 41455, mean latitude 17.3°N, mean longitude 94.3°E. (b) as (a) but for $O_2(^1\Delta)$ band. (c) as (a) but with background correction applied. (d) as (b) but with background correction applied.

2.4 Retrieval

To invert the observed radiation to spectral emission rates, we set up 30 layers around the Earth, such that each layer is centered at one tangent height. We denote the observed spectral radiances by $\mathbf{Y}$, the path length of each of the observed line of sights through each of the atmospheric layers by $\mathbf{L}$, and the emission rate from the layer by $\mathbf{X}$. Assuming no self-absorption, this yields the linear relation (2):

$$\mathbf{Y} = \mathbf{LX}\,. \tag{2}$$

In equation (2), dim($\mathbf{Y}$) = number of atmospheric layers × number of spectral points = 30×144 for the $O_2(^1\Sigma)$ band and 30×210 for the $O_2(^1\Delta)$ band. Dim($\mathbf{L}$) = number of the atmospheric layers × number of tangent heights in each scan = 30×30. Dim($\mathbf{X}$) = number of atmospheric layers × number of spectral points in the corresponding wavelength interval = 30×144 for $O_2(^1\Sigma)$ and 30×210 for $O_2(^1\Delta)$.
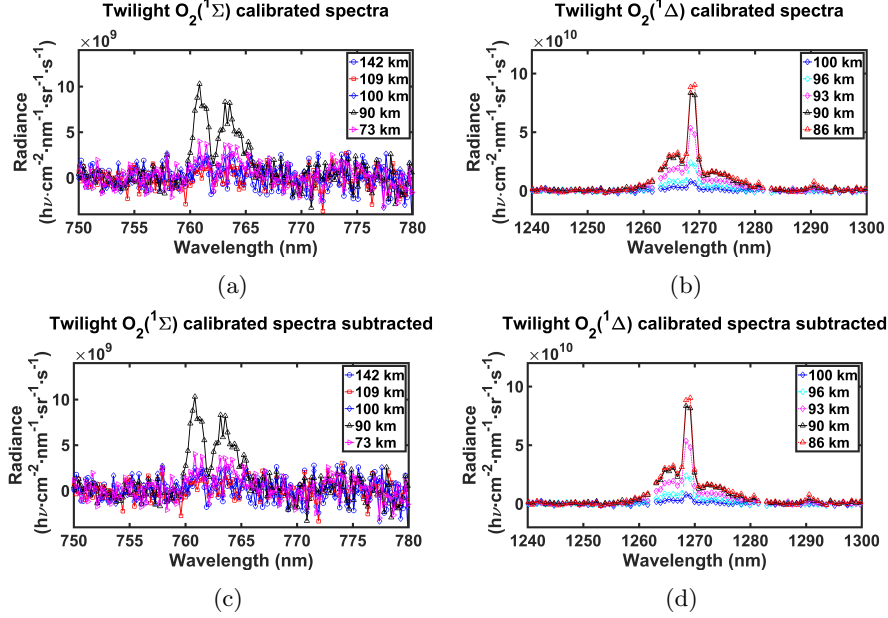
Figure 3. Examples of the twilight calibrated spectra, and the spectra from which the background $O_2(^3\Sigma_g)$ to $O_2(^1\Sigma)$ absorption has been subtracted. (a) for the 03/02/2010, orbit number 41455, mean latitude of 78.0°N, mean longitude of 226.5°E for $O_2(^1\Sigma)$ band. (b) as (a) but for the $O_2(^1\Delta)$ band. (c) as (a) but with background subtracted. (d) as (b) but with background subtracted.

We solve equation (2) by minimizing $||\mathbf{Y} - \mathbf{LX}||^2$ using standard least squares and normalization with the error covariance matrix $\mathbf{S}_y$, and obtain the inverted spectral emission intensity $\mathbf{X}$:

$$\mathbf{X} = (\mathbf{L}^T \mathbf{S}_y^{-1} \mathbf{L})^{-1} \mathbf{L}^T \mathbf{S}_y^{-1} \mathbf{Y} \ . \tag{3}$$

The error covariance matrix $\mathbf{S}_y$ has diagonal elements of the out-of-band variances of the background-corrected spectra in each altitude.

3 Results

3.1 Inverted spectra

Using our method in section 2.4, the emission intensities are calculated for the spectra described in sections 2.2 and 2.3. Examples of the emission intensity for daytime $O_2(^1\Sigma)$ are shown in Figure 4a and for daytime $O_2(^1\Delta)$ in Figure 4b.

The spectral shape of the $O_2(^1\Sigma)$ band in the daytime $O_2(^1\Sigma)$ spectra, and of the $O_2(^1\Delta)$ band in the daytime $O_2(^1\Delta)$ spectra are clearly visible. We find that the largest values for the daytime $O_2(^1\Sigma)$ band are located at about 90 km altitude, and for the $O_2(^1\Delta)$ band at 54 km, noting that the SCIAMACHY MLT scan range is 50 to 150 km. We also note that the maximum $O_2(^1\Delta)$ emission intensities in each limb scan, are about two orders of magnitude larger than the maximum values

5 of the $O_2(^1\Sigma)$ band in the corresponding limb scan.

Figure 4c shows the twilight $O_2(^1\Sigma)$ emission intensity, and Figure 4d shows the twilight $O_2(^1\Delta)$ emission intensity for the same orbit but retrieved from one of the three twilight MLT scans (see section 2.3). The $O_2(^1\Sigma)$ band is about one order of magnitude smaller than during daylight. The twilight $O_2(^1\Delta)$ band signal is more pronounced, but about two orders of magnitude smaller than during the day. The error bars in the panels of Figure 4 represent the square root of each of the diagonal

10 elements of the retrieval error covariance matrix $\mathbf{S}_a$ for each altitude:

$$\mathbf{S}_a = \mathbf{G}\mathbf{S}_y\mathbf{G}^T \tag{4}$$

in which the contribution function matrix $\mathbf{G}$ is defined as:

$$\mathbf{G} = (\mathbf{L}^T\mathbf{S}_y^{-1}\mathbf{L})^{-1}\mathbf{L}^T\mathbf{S}_y^{-1}. \tag{5}$$

Evaluating all altitudes, not shown here but indicated in Figure 4a, we observe the strongest signal of daytime $O_2(^1\Sigma)$ around

15 83–99 km. Hereafter, we use the term 'significant' for data with a signal to noise ratio of greater than one.

Figure 4c shows that the twilight $O_2(^1\Sigma)$ band emission intensities have large noise masking the signal. The daytime $O_2(^1\Delta)$ emission intensities are in general of higher SNR than the twilight $O_2(^1\Delta)$ emission intensities. The daytime $O_2(^1\Delta)$ emission intensities are strongest at the lowest observable altitudes, i.e., 54 km (Figure 4b). The strongest twilight $O_2(^1\Delta)$ emissions are located in the 83–96 km altitude range (Figure 4d shows only a selection of altitudes).

20 ## 3.2 Volume emission rates

We integrate the spectral emission intensity from 759 nm to 767 nm to obtain the $O_2(^1\Sigma)$ band integrated volume emission rate. Volume emission rate profiles for one sample satellite orbit (41455 on 03/02/2010) for daytime $O_2(^1\Sigma)$ and $O_2(^1\Delta)$ are shown in Figure 5a and Figure 5b respectively. Examples of the volume emission rate latitude-altitude distributions for the same orbit for daytime $O_2(^1\Sigma)$ are shown in Figure 6a and for daytime $O_2(^1\Delta)$ in Figure 6b. The blank regions represent

25 areas with signal to noise ratios of less than one.

The $O_2(^1\Sigma)$ VER has its maximum in the 90–98 km altitude range which is two orders of magnitude smaller than the $O_2(^1\Delta)$ maximum VER, as shown in Figure 5a. The volume emission rate profile of dayglow $O_2(^1\Delta)$ observed by TIMED/SABER, often has its maximum around 50 km altitude, as shown for example in Figure 1 of Mlynczak et al. (2007). Figure 5b shows that the SCIAMACHY MLT volume emission rate profiles are largest at the bottom of the observed altitude range, around

30 54 km. These VER profiles sometimes show secondary maxima in the range 80–90 km, which are at least one order of magnitude smaller than the largest SCIAMACHY VER. This secondary maximum occurs especially around equinox times. The measurement errors of the volume emission rates (not shown here) for different orbits show that the $O_2(^1\Sigma)$ volume
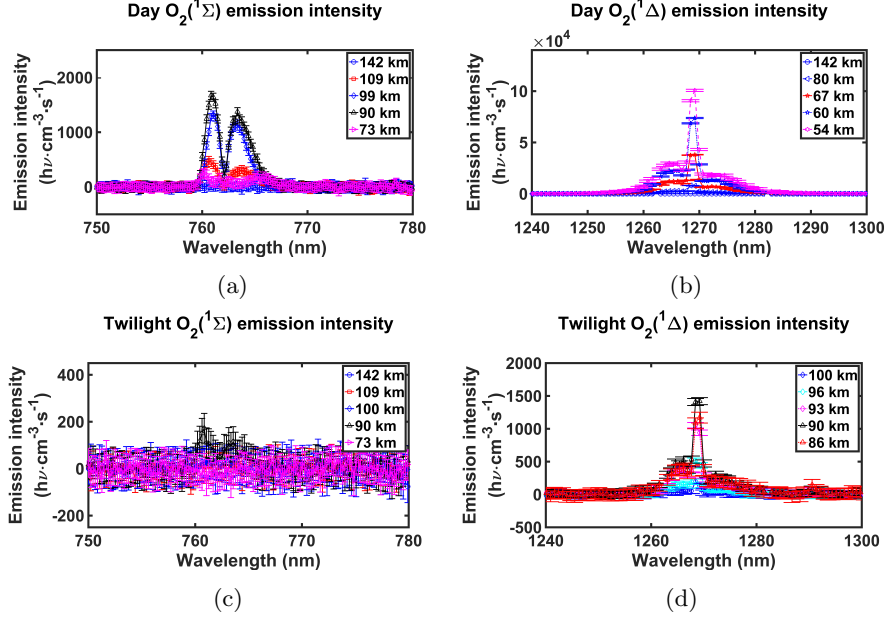
Figure 4. Examples of the emission intensities that are obtained by solving eq. (3). (a) for the daytime $O_2(^1\Sigma)$ band, on the date 03/02/2010, orbit number 41455, mean latitude of 17.3°N, mean longitude of 94.3°E. (b) as (a) but for $O_2(^1\Delta)$ band. (c) for the twilight $O_2(^1\Sigma)$ band on the date 03/02/2010, orbit number 41455, mean latitude 78.0°N, mean longitude 226.5°E. (d) as (c) but for $O_2(^1\Delta)$ band. Error bars represent the retrieval errors.

emission rates are significant from 65 to 140 km, and do not depend on latitude. Inspecting the volume emission rate altitude profiles (not shown here), we see that the $O_2(^1\Sigma)$ volume emission rates have largest SNR below 125 km and above 85 km.The best signal of the $O_2(^1\Delta)$ VER is below 95 km.

In a region above the South Atlantic and off the Brazilian coast, the Earth's magnetic field is anomalously low and the ionizing radiation can be increased by several orders of magnitude. This region is called the South Atlantic Anomaly (SAA, see for example Kurnosova et al. (1962)) and any spacecraft which crosses this region can give false instrument readings. In our retrievals, the SNR of the volume emission rates in the orbits that cross this region are affected by the SAA. The most dramatic influence of the SAA on our dataset is on the $O_2(^1\Sigma)$ volume emission rates SNR, although the values are still significant in the 80-100 km altitude range. The SAA influences the $O_2(^1\Sigma)$ measurements more than the $O_2(^1\Delta)$ measurements.

(a)   (b)
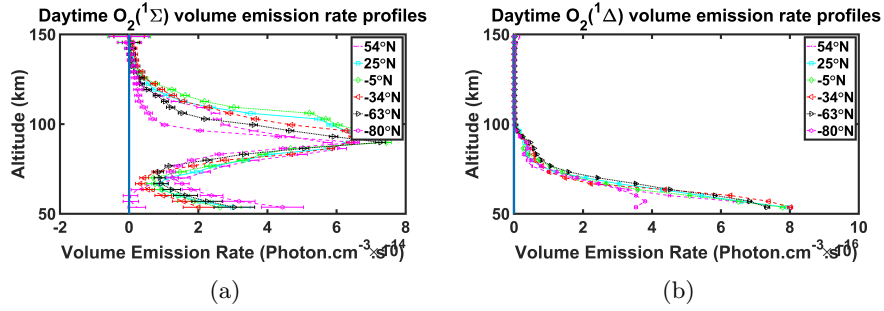
Figure 5. Typical profiles of the VER for different latitudes. (a) for daytime $O_2(^1\Sigma)$ VER, on the date 03/02/2010, orbit number 41455. (b) as (a) for daytime $O_2(^1\Delta)$ band. Error bars represent the retrieval errors.

3.3 Daily mean VER latitude-altitude distributions

We calculate the daily mean VERs as follows. We bin the measurements into 5° latitude bins. In each bin, the measurements located within $\pm 2.5°$ are attributed to that latitude, and averaged to daily mean VER. An example of the daily mean daytime $O_2(^1\Sigma)$ VER latitude-altitude distribution (on 03/02/2010) is shown in Figure 6c and of the daily mean daytime $O_2(^1\Delta)$ VER in Figure 6d (VERs with low signal to noise ratios and with large measurement errors are excluded). The daily mean $O_2(^1\Sigma)$ VERs have maximum values of about 1–2 orders of magnitude smaller than $O_2(^1\Delta)$. Similar to our results for a single orbit (section 3.2), we observe the largest $O_2(^1\Delta)$ VER below 60 km and the largest $O_2(^1\Sigma)$ VER at 90 km.

To assess the signal to noise ratio for the daytime VERs, Figure 6e shows the daily mean $O_2(^1\Sigma)$ VERs signal to noise ratios. We observe the strongest signal of daytime $O_2(^1\Sigma)$ in the 70–130 km altitude range. The strongest signal of the twilight $O_2(^1\Sigma)$ is observed between 84 km and 95 km (not shown here). Figure 6f shows that the stronger signal of daytime $O_2(^1\Delta)$ is observed below 105 km, with the strongest around 70 km. The largest signal of twilight $O_2(^1\Delta)$ is observed in the altitude range of 83–97 km (not shown).

3.4 Time series

In the following, we discuss the variation of the daily mean VERs versus latitude and time. First we will discuss the temporal variation in the mesosphere and lower thermosphere (70–140 km) at 30°N. Thereafter we will discuss the variation of the peak values, peak altitudes, and centroid altitudes as a function of time and latitude.

3.4.1 Time series at 30°N

By calculating the daily mean VERs for all of the days on which SCIAMACHY MLT limb scans are available, we obtain time series of the daily mean VERs from 07/2008 to 03/2012. An example of these time series of the daily mean daytime $O_2(^1\Sigma)$
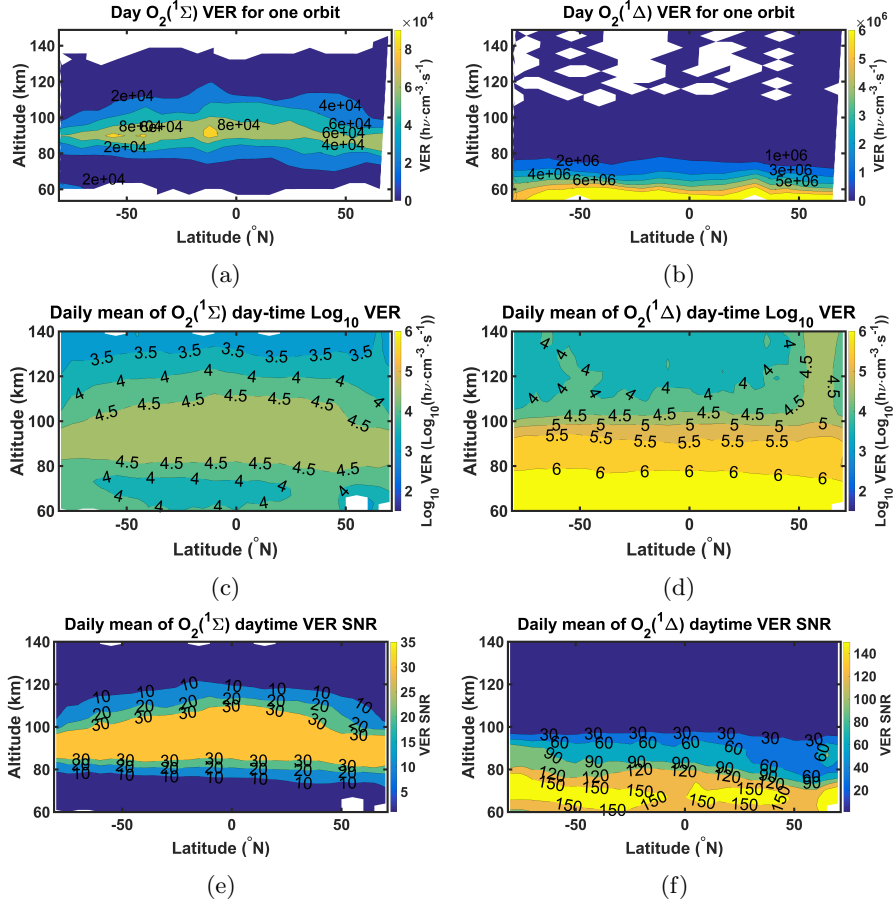
Figure 6. Latitude-altitude contours of the daytime VER. (a) for one satellite orbit, the $O_2(^1\Sigma)$ band, date: 2010/02/03, orbit number: 41455. (b) as (a) for $O_2(^1\Delta)$. Signal to noise ratios less than one and large noisy values are excluded. (c) and (d) as (a) and (b) respectively, averaged on the all of the orbits on the whole day of 03/02/2010, with the same logarithmic scale. Negative values are excluded. (e) Signal to noise ratios of the daily mean of $O_2(^1\Sigma)$ VERs. Areas where the signal to noise ratio is less than 1 are plotted in white. (f) as (e) for $O_2(^1\Delta)$ band.
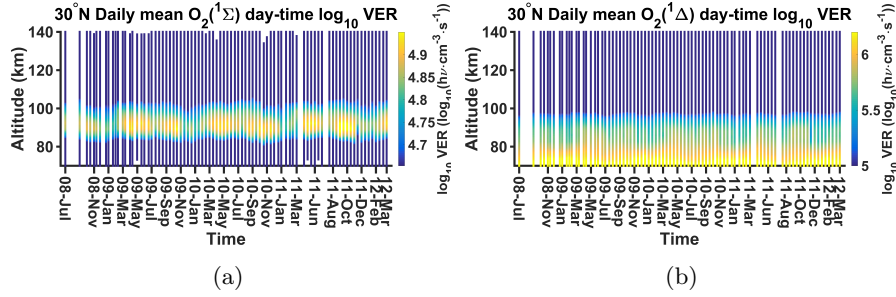
Figure 7. Time series of the daily mean VER. (a) for daytime $O_2(^1\Sigma)$ VER, 30°N, 07/2008 to 03/2012. (b) as (a) for daytime $O_2(^1\Delta)$ band.

VER, chosen for 30°N from all altitudes combinations is shown in Figure 7a, and for the daytime $O_2(^1\Delta)$ VER of the same location in Figure 7b.

We found a semi-annual variation with the strongest $O_2(^1\Sigma)$ signal in the 90-95 km range during May-June and September-November, and the lowest signal in December-March, with a secondary minimum in August. The highest values of the $O_2(^1\Delta)$

5 VER are located at the lowest altitude of observations, formed mostly by ozone photodissociation (Thomas et al., 1984). We observe secondary maximum values which mostly occur in May-June and September-November (approximately spring and autumn) in the 75–95 km altitude range. The secondary maximum of $O_2(^1\Delta)$ occurs in the same altitude range and with the same temporal variation as the $O_2(^1\Sigma)$ signal. This will be investigated in more detail in the following section.

3.4.2 Variation of peak values

10 Next we evaluate the variations of the maximal daily mean VERs in the mesosphere and lower thermosphere with respect to latitude and time. For this, we derive the maximal values from the daily mean VERs for $O_2(^1\Sigma)$ and between 85–100 km altitude for $O_2(^1\Delta)$, which are shown in Figures 8a and 8b respectively. Only those regions are shown in Figures 8b, 8d, and 8f where the secondary maxima of $O_2(^1\Delta)$ exist. The peak altitudes are also obtained at the same time and will be discussed in section 3.4.3. The maxima of the $O_2(^1\Sigma)$ VER at middle to low latitudes (60°S–60°N) appear to be correlated

15 with the maximum intensity of solar radiance. Additionally, we observe sometimes attenuations in the maximum values in the late northern winters, mostly from late January until early March of each year. Also there are some high values at northern polar latitudes: in spring 2009, from autumn to spring 2009–2010, from autumn to winter 2010, and from autumn to spring 2011–2012.

The secondary maxima of the $O_2(^1\Delta)$ VER are confined to winter at mid-to-high latitudes.

20 The correlation of the $O_2(^1\Sigma)$ VERs with the solar radiance suggests formation caused by solar light, either by ozone photolysis (R2) and (R7), or caused by larger abundances of atomic oxygen owing to stronger O_2 photolysis. In the second case, the formation of the excited states could also be due to the recombination of atomic oxygen (R1) and (R6). The maximal

values at high latitudes, where the solar flux is low, in general suggest other sources such as recombination of atomic oxygen (Thomas et al., 1984). This is true in particular for $O_2(^1\Sigma)$, where high values occur at high latitudes in winter and spring; these are probably caused by downward transport of thermospheric atomic oxygen into the mesosphere / lower thermosphere.

There are two possibilities for secondary maxima of $O_2(^1\Delta)$. They happen in the region where the secondary ozone maximum is strongest. Also, atomic oxygen densities might be strongest due to enhanced mixing with the lower thermosphere. Detailed study of the processes which result in the formation of the secondary maxima of $O_2(^1\Delta)$ is beyond our work.

3.4.3 Variation of peak altitudes

The altitudes of the peak values of $O_2(^1\Sigma)$ and $O_2(^1\Delta)$ are shown in Figures 8c and 8d. The altitudes of the peak values of $O_2(^1\Sigma)$ roughly follows the maximum intensity of solar radiance, but shows highest values at low-to middle latitudes. We refer to the maximum intensity of solar radiance as the latitudes and times in which solar zenith angles have their lowest values in. The low values of the maximum VERs, and the high altitudes of the maximal VERs at the outermost high latitudes in the northern winters, correspond to low signal to noise ratios and are below our significance level.

In the regions where the secondary maxima of $O_2(^1\Delta)$ happen, the peak altitudes occur in ~84–89 km altitude range.

3.4.4 Centroid altitudes

The estimation of the peak altitude is affected by instrument noise and vertical resolution. A more stable measure is the centroid altitude h_{CA}:

$$h_{CA} = \frac{\sum_i a_i v_i}{\sum_i v_i} , \qquad (6)$$

where v_i is the volume emission rate at altitude a_i, which ranges from ~50 km to ~150 km for $O_2(^1\Sigma)$ and from ~85 km to ~100 km for $O_2(^1\Delta)$. Figure 8e shows the centroid altitude for daytime $O_2(^1\Sigma)$ and Figure 8f for daytime $O_2(^1\Delta)$.

The maximum h_{CA} of the $O_2(^1\Sigma)$ band are correlated with the (maximum intensity) of solar radiance. We also observe maximal values of h_{CA} in a narrow band at northern polar latitudes, where the solar flux generally is low. This also suggests recombination of atomic oxygen as a source, as discussed in the subsection 3.4.2. The very low values of the h_{CA}s, at the highest latitudes, mostly in the hemispheric wintertimes, correspond to low signal to noise ratios of the corresponding VERs (not shown here), and below our significance level.

The $O_2(^1\Delta)$ secondary maximums occur in winter at high latitudes. The values of the $O_2(^1\Delta)$ h_{CA} range between ~88 km and ~89 km altitude.

Figures 8c, 8d, and 8f, show a decrease in the altitude of the maximum $O_2(^1\Sigma)$, altitude of the maximum $O_2(^1\Delta)$, and $O_2(^1\Delta)$ h_{CA}, respectively between November 2010 and February 2011. This is due to a change in the limb sequence so that tangent altitudes were shifted, as seen for example at lower altitudes in these days. However, this doesn't have any notable effect on the VER time series in Figures 7a ,7b, 8a, and 8b.
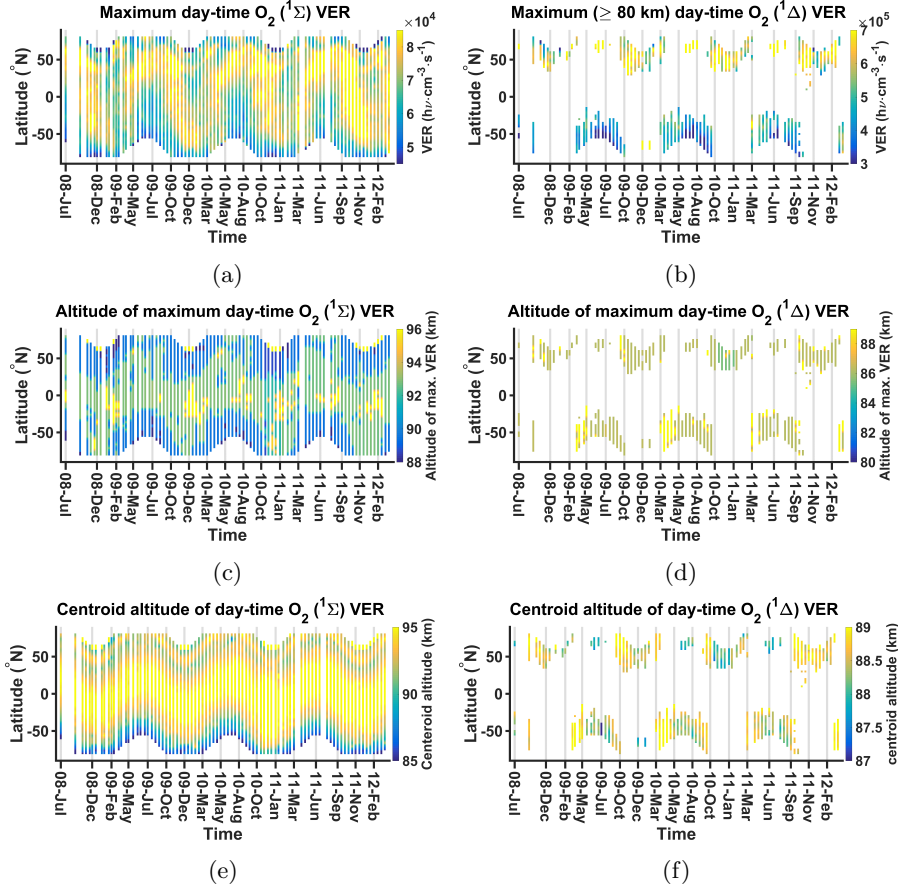
Figure 8. (a) Time series of the maximal daily mean $O_2(^1\Sigma)$ VER. (b) as (a) for $O_2(^1\Delta)$ band. (c) Time series of the altitudes of the maximum daily mean $O_2(^1\Sigma)$ VER. (d) as (c) for $O_2(^1\Delta)$ band. (e) Time series of the centroid altitudes of the daytime $O_2(^1\Sigma)$ daily mean VER (km). (f) as (e) for $O_2(^1\Delta)$ band.

3.4.5 Discussion of temporal-spatial variation

The temporal-latitudinal variation in peak values and altitudes suggests that $O_2(^1\Sigma)$ at 85–100 km altitude is formed by a combination of ozone photolysis and atomic oxygen recombination. At high latitudes during winter and spring, atomic oxygen
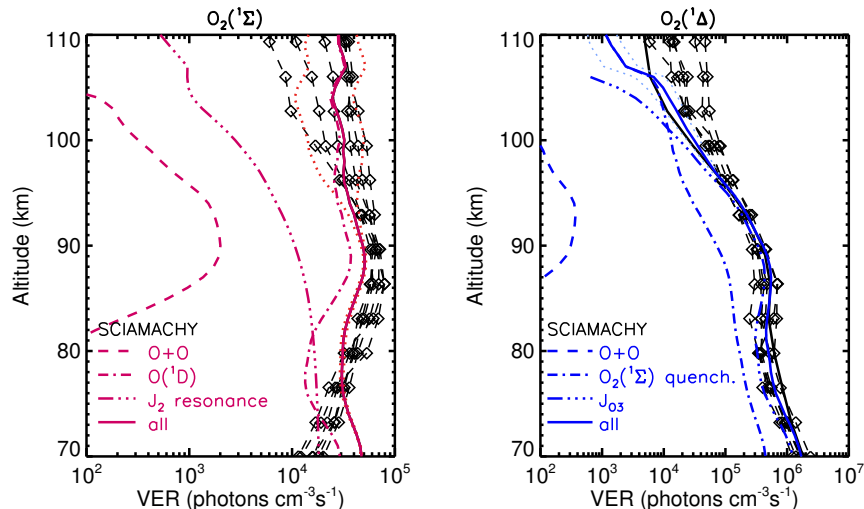
Figure 9. Modeled VERs of $O_2(^1\Sigma)$ (left) and $O_2(^1\Delta)$ (right). Solid lines are the mean of all model results for solar zenith angles 0, 10, 20, 30, 40, 50, 60, 70, 80, 88° considering all formation processes; dotted lines show the variability due to photolysis reactions ($\pm$ standard deviation). The dashed, dash-dotted, and dash-dot-dot lines show the contributions of individual formation processes: $O + O$, $O(^1D)$ quenching and resonant excitation for $O_2(^1\Sigma)$, $O + O$, $O_2(^1\Sigma)$ and ozone photolysis for $O_2(^1\Delta)$. Black lines with symbols are SCIAMACHY profiles at five latitudes observed on February 3, 2010 (see Figure 5).

recombination dominates, but in the sub-solar region, ozone photolysis is more important. In contrast, the secondary peak of $O_2(^1\Delta)$ stems mainly from atomic oxygen recombination, in particular at high latitudes during winter.

The temporal-latitudinal variation in peak values and altitudes suggests that the daytime VERs of $O_2(^1\Delta)$ and $O_2(^1\Sigma)$ in the altitude range of 80–100 km are formed by a combination of ozone and O_2 photolysis and atomic oxygen recombination.

5 At high latitudes during winter and spring, atomic oxygen recombination dominates, but in the sub-polar region, photolysis of ozone and O_2 is more important.

To test whether these conclusions are generally consistent with our understanding of the photochemical production and loss of $O_2(^1\Delta)$ and $O_2(^1\Sigma)$, a simple photochemical model covering the production and loss reactions summarized in Section 1 (R1 to R15) was set up. Photochemical equilibrium was considered for $O_2(c^1\Sigma_u^-)$, $O(^1S)$, $O(^1D)$, $O_2(^1\Delta)$, and $O_2(^1\Sigma)$.

10 Reaction rates were taken from the JPL recommendation (Burkholder et al., 2015) with the exception of the quenching of the intermediate $O_2(c^1\Sigma_u^-)$ state (the q6 and q7 rates shown in Figure 1), which was taken from (Stegman and Murtagh, 1991) with δ coefficients from (Bates, 1988). Einstein coefficients for the $O_2(^1\Sigma) \rightarrow O_2(X^3\Sigma_g^-)$ transition (A_2 in Figure 1) were taken from Mlynczak and Solomon (1993), for the $O(^1S) \rightarrow O(^1D)$ transition (A_4 in Figure 1) was taken from NIST atomic spectra database [2], for the $O(^1S) \rightarrow O(^3P)$ transition (A_5 in Figure 1) was taken from NIST atomic spectra database, and

15 for the O_2^* products (not given in Figure 1) were taken from Stegman and Murtagh (1991). Photolysis rates for solar zenith

---
[2]www.nist.gov

angles 0, 10, 20, 30, 40, 50, 60, 70, 80 and 88° were calculated using a fixed ozone profile using the 3dCTM model (Sinnhuber et al., 2012). The rate of photoexcitation of the ground state $O_2(X^3\Sigma_g^-)$ to the second excited state $O_2(^1\Sigma)$ was calculated following (Bucholtz et al., 1986) but using recent line-strength provided by the HITRAN database at hitran.org (Rothman et al., 2013), yielding a rate of 2.04×10^{-9} photons cm^{-3} s^{-1} above 70 km. Temperature, total air density, and the densities of O_2

5 and N_2 were taken from the NRLMSISE-00 model (Picone et al., 2002) at 10:00 local time at the equator. The production of $O(^1D)$ by photolysis of H_2O and CO_2 in the Ly-α range was also considered, and H_2O and CO_2 were assumed to have constant mixing ratios of 1 ppm (H_2O) and 380 ppm (CO_2). Ozone density was prescribed adapted from a multi-year global average of SABER data in the altitude region 70–104 km (see Smith et al. (2013), Figure 3). Atomic oxygen was calculated from photochemical equilibrium of ozone considering only ozone photolysis and production by $O + O_2$. The resulting VERs

10 of $O_2(^1\Delta)$ and $O_2(^1\Sigma)$ are shown in Figure 9, compared to the SCIAMACHY daytime data of February 3, 2010 shown in Figure 5). Considering that the ozone profile, O_2, N_2 and temperature are not chosen to fit those specific observations, the agreement is very good for both emissions, indicating that the main processes of $O_2(^1\Delta)$ and $O_2(^1\Sigma)$ formation and loss are reproduced well by this simple model. Also shown are the contributions of the individual production reactions: $O + O$, quenching of $O(^1D)$, and resonance excitation of $O_2(X^3\Sigma_g^-)$ for $O_2(^1\Sigma)$, $O + O$, quenching of $O(^1\Sigma)$, and ozone photolysis

15 for $O_2(^1\Delta)$.

Below about 82 km, $O_2(^1\Sigma)$ is formed in about equal amounts by quenching of $O(^1D)$, while above, quenching of $O(^1D)$ dominates. The reaction of $O + O$ contributes about one order of magnitude less $O_2(^1\Sigma)$ than the other two branches even in the region where it has the largest contribution (around 90 km). This is consistent with the ratio of emission intensities during twilight and during daytime of about a factor of ten as discussed in Section 3.1, considering that during night-time and twilight,

20 $O_2(^1\Sigma)$ is formed solely by the $O + O$ reaction. The formation of $O_2(^1\Delta)$ is dominated by ozone photolysis at all altitudes, though below 90 km, $O_2(^1\Sigma)$ quenching contributes about 10–25%.

$O(^1D)$ is formed mainly by photolysis of O_3 in the below 90 km, by photolysis of O_2 above that altitude. During daytime, the formation of both the $O_2(^1\Delta)$ and $O_2(^1\Sigma)$ states are formed photolysis in agreement with our observation that the peak maxima correlate with the maximum intensity of solar radiance. The contribution of the $O + O$ reaction generally is smaller

25 by one to three orders of magnitude than the contribution of photolysis, in agreement with the lower VERs observed during twilight when photolysis is not a significant production process. However, it should be pointed out that the relation between the O_2 airglow and atomic oxygen by the $O + O$ reaction and de-excitation of the excited intermediate states such as $O_2(c^1\Sigma_u^-)$ is probably quadratic to cubic; increased amounts of atomic oxygen, e.g. at high latitudes during winter when large amounts of atomic oxygen can be transported or mixed down from the lower thermosphere, can therefore increase the contribution of the

30 $O + O$ reaction to the overall airglow considerably. This explains the observed enhancements of the airglow at high Northern latitudes in winter and spring, in particular as the centroid altitudes in these occasions range around 90 km, the altitude where the $O + O$ reaction has the strongest influence.

3.5 Relationship between the VER time series variations and sudden stratospheric warmings - example

Sudden Stratospheric Warmings (SSWs) are dynamical phenomena in the winter polar stratosphere caused by upward propagating planetary waves interacting with the mean flow (Matsuno, 1971). During the so-called recovery phase of SSWs, the reformation of the jet changes gravity wave propagation to the mesosphere. The induced change in the residual circulation results in an enhanced descent of air. This causes adiabatic warming and the stratopause reforms at altitudes as high as 75–80 km (Siskind et al., 2010). The unusual brightening of the OH airglow (Winick et al., 2009) presumably caused by enhanced downwelling of atomic oxygen. According to Harada et al. (2010), a major SSW event happened around 21 January 2009 (Figure 1 of that paper). We therefore expect to observe enhanced airglow at the end of January 2009.

Based on the temporal evolution of mesospheric temperature during the SSW event, Gao et al. (2011b) divided the response in the mesosphere into three stages: prior to day 15 is considered the normal stage; days 15–22 correspond to the cooling stage; days post 22 correspond to the recovery stage. According to this, they reported that the O_2 nightglow brightness decreased by about a factor of 10 during the cooling stage and then increased by about a factor of 3 during the recovery stage relative to the normal stage. Figures 10a and 10b show the time series from 12/2008 to 04/2009 of the daytime $O_2(^1\Sigma)$ and $O_2(^1\Delta)$ daily mean VER, averaged from 60°N to 70°N. We observe that on the last day of the cooling stage, i.e., 22 January 2009, the daily zonal mean $O_2(^1\Sigma)$ and $O_2(^1\Delta)$ VERs show a reduced maximum intensity in the 82–87 km altitude range. We observe larger intensities on the next measurement day of SCIAMACHY about three weeks later, i.e., on 10 February 2009. This is expected from a decrease of atomic oxygen due to horizontal mixing and upwelling during the cooling stage, and then downward extension of the MLT region with large mixing ratio of O during the recovery stage of the SSW (Gao et al., 2011b). On the measurement day of SCIAMACHY after the recovery phase, i.e. 23 March 2009, the relative difference in the $O_2(^1\Delta)$ signal is less prominent compared to the relative difference in $O_2(^1\Sigma)$. A detailed analysis of this relationship is beyond the scope of this paper.

We also note that the signal to noise ratios of the VERs for $O_2(^1\Sigma)$ shown in Figure 10c is statistically significant. It is shown in Figure 10d that during and after the initial stage of the SSW event, the $O_2(^1\Delta)$ signal becomes weaker and stronger respectively, and the signal to noise ratio of the data are such that this behaviour is statistically significant.

4 Discussion and conclusions

We present the retrieval of daytime and twilight $O_2(^1\Sigma)$ and $O_2(^1\Delta)$ spectral emissions from MLT measurements of the airglow in limb viewing geometry from the SCIAMACHY instrument on-board Envisat. From the retrieved spectra, we calculate the band integrated VERs for both bands. The maxima of the $O_2(^1\Sigma)$ VER and the centroid altitude of the $O_2(^1\Sigma)$ are correlated with the maximum intensity of solar radiance. High values of maximum VER and centroid altitude are additionally seen at northern polar latitudes. The (30°N) time series of $O_2(^1\Sigma)$ VER shows a maximum in the 90–98 km altitude range. The maximum values correspond to high centroid altitudes for $O_2(^1\Sigma)$. The daily zonal (60°N–70°N) mean $O_2(^1\Sigma)$ VER show a reduced maximum intensity in the 82–87 km, in the initiation of the sudden stratospheric warming-2009 event, and an increase in intensity about three weeks later.
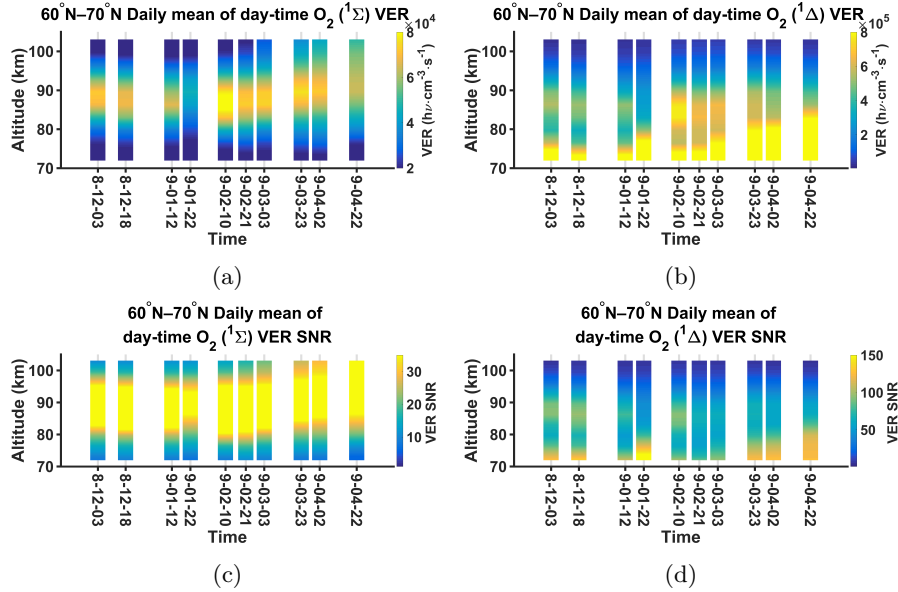
Figure 10. (a) Daily mean of the daytime $O_2(^1\Sigma)$ VER from date: 12/2008 to date: 04/2009 averaged between $60°$N and $70°$N latitude. (b) as (a) for $O_2(^1\Delta)$ band. (c) Daily mean of the signal to noise ratios of the daytime $O_2(^1\Sigma)$ VER from date: 12/2008 to date: 04/2009 averaged between $60°$N and $70°$N latitude. (d) as (c) for $O_2(^1\Delta)$ VER signal to noise ratios.

The maxima of the $O_2(^1\Delta)$ VER are also correlated with the maximum intensity of solar radiance. They are most prominent in summer, while the altitudes of the maximal values have their highest values in winter, both occur at high latitudes. The time series of $O_2(^1\Delta)$ VER is two orders of magnitude larger than $O_2(^1\Sigma)$ VER at its maximal values which are located below the observation altitude (<60 km), but it shows some secondary maxima with about one order of magnitude smaller than the primary maxima at 84-89 km. This happens in winter at high latitudes. The maximum VERs correspond to the low centroid altitudes for the $O_2(^1\Delta)$ band. The daily zonal ($60°$N–$70°$N) mean $O_2(^1\Delta)$ VERs show a reduced maximum intensity of 82–87 km, in the initiation of the sudden stratospheric warming-2009 event, and an increase in intensity about three weeks later, although the relative difference in $O_2(^1\Delta)$ band signal is less prominent compared to the relative difference in $O_2(^1\Sigma)$.

The intensification of the VER during the sudden stratospheric warming in early 2009 presumably corresponds to the downwelling of the atomic oxygen following the warming, while the decrease is probably due to up-welling as well as horizontal mixing during the warming event.

Our results suggest that at low and middle latitudes $O_2(^1\Sigma)$ and $O_2(^1\Delta)$ abundances during daytime are dominated by photolysis of ozone below 90 km, by photolysis of ozone and O_2 above 90 km as supported by our observed correlation with

solar illumination, and consistent with the processes depicted in Figure 1. At high latitudes however, in particular during winter, atomic oxygen abundances might be a more important driver due to the recombination of $O + O$ and subsequent de-excitation via $O(^1S)$ and $O_2(^1\Sigma)$.

As the formation of the $O_2(^1\Delta)$ band is dominated by ozone photolysis, this band can be used to derive ozone densities directly. However, as quenching of $O_2(^1\Sigma)$ contributes about 10–25% to the overall production in 70–90 km, the accuracy of this retrieval can be improved considerably when both lines are available. The $O_2(^1\Sigma)$ band is dominated by quenching of $O(^1D)$, and daytime $O(^1D)$ can be derived from observations of the $O_2(^1\Sigma)$ VER. However, below $\sim$90 km, the resonant excitation from the ground state has to be taken into account as well. The rate used here based on new line strength data from HITRAN is lower by about a factor of two compared to a similar estimate used for HRDI data as described in (Marsh et al., 2002), and lower by about a factor of four compared to the original estimate by (Bucholtz et al., 1986). We conclude that the retrieval of $O(^1D)$ and ozone as the main source of $O(^1D)$ below 90 km from $O_2(^1\Sigma)$ is possible, but needs a careful estimation of the rate of resonant excitation.

Acknowledgements. Amirmahdi Zarboo and Miriam Sinnhuber gratefully acknowledge funding by BMBF grant 01LG1208A (ROMIC-MesoEnergy). The support of BMBF ROMIC project for the University of Bremen is also gratefully acknowledged. The SCIAMACHY project was funded by Germany with support from the Netherlands and Belgium as a national contribution to ESA Envisat. The authors also acknowledge the reviewers for the very constructive comments on the paper.

References

Barth, C. A.: Three-body reactions, in: Annales de Geophysique, vol. 20, p. 182, 1964.

Barth, C. A. and Hildebrandt, A. F.: The 5577 A airglow emission mechanism, Journal of Geophysical Research, 66, 985–986, 1961.

Bates, D.: The green light of the night sky, Planetary and Space Science, 29, 1061–1067, doi:10.1016/0032-0633(81)90003-9, 1981.

Bates, D.: Excitation and quenching of the oxygen bands in the nightglow, Planetary and space science, 36, 875–881, 1988.

Bates, D.: Nightglow emissions from oxygen in the lower thermosphere, Planetary and Space Science, 40, 211 – 221, doi:10.1016/0032-0633(92)90059-W, 1992.

Bovensmann, H., Burrows, J. P., Buchwitz, M., Frerick, J., Noël, S., Rozanov, V. V., Chance, K. V., and Goede, a. P. H.: SCIAMACHY: Mission Objectives and Measurement Modes, Journal of the Atmospheric Sciences, 56, 127–150, 1999.

Brasseur, G. P. and Solomon, S.: Aeronomy of the middle atmosphere: chemistry and physics of the stratosphere and mesosphere, vol. 32, Springer Science & Business Media, 2006.

Bucholtz, A., Skinner, W., Abreu, V. J., and Hays, P.: The dayglow of the O 2 atmospheric band system, Planetary and space science, 34, 1031–1035, 1986.

Burkholder, J., Sander, S., Abbatt, J., Barker, J., Huie, R., Kolb, C., Kurylo, M., Orkin, V., Wilmouth, D., and Wine, P.: Chemical Kinetics and Photochemical Data for Use in Atmospheric Studies–Evaluation Number 18, Nasa panel for data evaluation technical report, 2015.

Burrows, J. P., Hölzle, E., Goede, A. P. H., Visser, H., and Fricke, W.: SCIAMACHY—scanning imaging absorption spectrometer for atmospheric chartography, Acta Astronautica, 35, 445–451, doi:10.1016/0094-5765(94)00278-T, 1995.

Christensen, A. B., Yee, J.-H., Bishop, R. L., Budzien, S. A., Hecht, J. H., Sivjee, G., and Stephan, A. W.: Observations of molecular oxygen Atmospheric band emission in the thermosphere using the near infrared spectrometer on the ISS/RAIDS experiment, Journal of Geophysical Research: Space Physics, 117, 2012.

DeMore, W. B.: Primary Processes in Ozone Photolysis, The Journal of Chemical Physics, 44, 1780, doi:10.1063/1.1726939, 1966.

Evans, W. F. J., Hunten, D. M., Llewellyn, E. J., and Jones, A. V.: Altitude profile of the infrared atmospheric system of oxygen in the dayglow, Journal of Geophysical Research, 73, 2885–2896, doi:10.1029/JA073i009p02885, 1968.

Gao, H., Xu, J., Chen, G., Yuan, W., and Beletsky, A. B.: Global distributions of OH and O2 (1.27 μm) nightglow emissions observed by TIMED satellite, Science China Technological Sciences, 54, 447–456, doi:10.1007/s11431-010-4236-5, 2011a.

Gao, H., Xu, J., Ward, W., and Smith, A. K.: Temporal evolution of nightglow emission responses to SSW events observed by TIMED/SABER, Journal of Geophysical Research: Atmospheres, 116, 2011b.

Greer, R., Llewellyn, E., Solheim, B., and Witt, G.: The excitation of O2 (b1Σg+) in the nightglow, Planetary and Space Science, 29, 383–389, 1981.

Harada, Y., Goto, A., Hasegawa, H., Fujikawa, N., Naoe, H., and Hirooka, T.: A Major Stratospheric Sudden Warming Event in January 2009, Journal of the Atmospheric Sciences, 67, 2052–2069, doi:10.1175/2009JAS3320.1, 2010.

Hays, P. B., Abreu, V. J., Dobbs, M. E., Gell, D. A., Grassl, H. J., and Skinner, W. R.: The high-resolution doppler imager on the Upper Atmosphere Research Satellite, Journal of Geophysical Research, 98, 10 713, doi:10.1029/93JD00409, 1993.

Huestis, D. L.: Current Laboratory Experiments for Planetary Aeronomy, pp. 245–258, American Geophysical Union, doi:10.1029/130GM16, 2013.

Khomich, V. Y., Semenov, A. I., and Shefov, N. N.: Airglow as an indicator of upper atmospheric structure and dynamics, doi:10.1007/978-3-540-75833-4, 2008.

Killeen, T. L., Wu, Q., Solomon, S. C., Ortland, D. A., Skinner, W. R., Niciejewski, R. J., and Gell, D. A.: TIMED Doppler Interferometer: Overview and recent results, Journal of Geophysical Research, 111, A10S01, doi:10.1029/2005JA011484, 2006.

Kirillov, A.: The calculation of quenching rate coefficients of O2 Herzberg states in collisions with CO2, CO, N2, O2 molecules, Chemical Physics Letters, 592, 103 – 108, doi:10.1016/j.cplett.2013.12.009, 2014.

5 Kirillov, A. S.: Model of vibrational level populations of Herzberg states of oxygen molecules at heights of the lower thermosphere and mesosphere, Geomagnetism and Aeronomy, 52, 242–247, doi:10.1134/S0016793212020077, 2012.

Kurnosova, L., Kolobyanina, T., Logachev, V., Razorenov, L., Sirotkin, I., and Fradkin, M.: Discovery of radiation anomalies above the South Atlantic at heights of 310–340 km, Planetary and Space Science, 9, 513–516, doi:10.1016/0032-0633(62)90057-0, 1962.

Lednyts'kyy, O., Von Savigny, C., Eichmann, K. U., and Mlynczak, M. G.: Atomic oxygen retrievals in the MLT region from SCIAMACHY
10   nightglow limb measurements, Atmospheric Measurement Techniques, 8, 1021–1041, doi:10.5194/amt-8-1021-2015, 2015.

Llewellyn, E. J., Lloyd, N. D., Degenstein, D. A., Gattinger, R. L., Petelina, S. V., Bourassa, A. E., Wiensz, J. T., Ivanov, E. V., McDade, I. C., Solheim, B. H., McConnell, J. C., Haley, C. S., von Savigny, C., Sioris, C. E., McLinden, C. A., Griffioen, E., Kaminski, J., Evans, W. F., Puckrin, E., Strong, K., Wehrle, V., Hum, R. H., Kendall, D. J., Matsushita, J., Murtagh, D. P., Brohede, S., Stegman, J., Witt, G., Barnes, G., Payne, W. F., Piché, L., Smith, K., Warshaw, G., Deslauniers, D. L., Marchand, P., Richardson, E. H., King, R. A., Wevers,
15   I., McCreath, W., Kyrölä, E., Oikarinen, L., Leppelmeier, G. W., Auvinen, H., Mégie, G., Hauchecorne, A., Lefèvre, F., de La Nöe, J., Ricaud, P., Frisk, U., Sjoberg, F., von Schéele, F., and Nordh, L.: The OSIRIS instrument on the Odin spacecraft, Canadian Journal of Physics, 82, 411–422, doi:10.1139/p04-005, 2004.

Marsh, D. R., Skinner, W. R., Marshall, A. R., Hays, P. B., Ortland, D. A., and Yee, J.-H.: High Resolution Doppler Imager observations of ozone in the mesosphere and lower thermosphere, Journal of Geophysical Research: Atmospheres, 107, 2002.

20 Matsuno, T.: A dynamical model of the stratospheric sudden warming, 1971.

Mlynczak, M., Morgan, F., Yee, J.-H., Espy, P., Murtagh, D., Marshall, B., and Schmidlin, F.: Simultaneous measurements of the O2 ($^1\Delta$) and O2 ($^1\Sigma$) Airglows and ozone in the daytime mesosphere, Geophysical research letters, 28, 999–1002, 2001.

Mlynczak, M. G. and Olander, D. S.: On the utility of the molecular oxygen dayglow emissions as proxies for middle atmospheric ozone, Geophysical Research Letters, 22, 1377–1380, doi:10.1029/95GL01321, 1995.

25 Mlynczak, M. G. and Solomon, S.: A detailed evaluation of the heating efficiency in the middle atmosphere, Journal of Geophysical Research: Atmospheres, 98, 10 517–10 541, 1993.

Mlynczak, M. G., Solomon, S., and Zaras, D. S.: An updated model for O 2 (a 1 Δg) concentrations in the mesosphere and lower thermosphere and implications for remote sensing of ozone at 1.27 μm, Journal of Geophysical Research: Atmospheres, 98, 18 639–18 648, doi:10.1029/93JD01478, 1993.

30 Mlynczak, M. G., Marshall, B. T., Martin-Torres, F. J., Russell, J. M., Thompson, R. E., Remsberg, E. E., and Gordley, L. L.: Sounding of the Atmosphere using Broadband Emission Radiometry observations of daytime mesospheric O2 (1Δ) 1.27 μm emission and derivation of ozone, atomic oxygen, and solar and chemical energy deposition rates, Journal of Geophysical Research: Atmospheres, 112, 2007.

Nicolet, M.: Aeronomic reactions of hydrogen and ozone, in: Mesospheric models and related experiments, pp. 1–51, Springer, 1971.

Picone, J., Hedin, A., Drob, D. P., and Aikin, A.: NRLMSISE-00 empirical model of the atmosphere: Statistical comparisons and scientific
35   issues, Journal of Geophysical Research: Space Physics, 107, 2002.

Rothman, L., Gordon, I., Babikov, Y., Barbe, A., Benner, D., Bernath, P., Birk, M., Bizzocchi, L., Boudon, V., Brown, L., et al.: The HITRAN 2012 Molecular Spectroscopic Database, 130, 4–50, J. Quant. Spectrosc. Ra., Elsevier, ISSN, pp. 0022–4073, 2013.

Sheese, P. E., Llewellyn, E. J., Gattinger, R. L., Bourassa, A. E., Degenstein, D. A., Lloyd, N. D., and McDade, I. C.: Temperatures in the upper mesosphere and lower thermosphere from OSIRIS observations of O2 A-band emission spectra, Canadian Journal of Physics, 88, 919–925, doi:10.1139/P10-093, 2010.

Shepherd, G. G., Thuillier, G., Gault, W. A., Solheim, B. H., Hersom, C., Alunni, J. M., Brun, J.-F., Brune, S., Charlot, P., Cogger, L. L., Desaulniers, D.-L., Evans, W. F. J., Gattinger, R. L., Girod, F., Harvie, D., Hum, R. H., Kendall, D. J. W., Llewellyn, E. J., Lowe, R. P., Ohrt, J., Pasternak, F., Peillet, O., Powell, I., Rochon, Y., Ward, W. E., Wiens, R. H., and Wimperis, J.: WINDII, the wind imaging interferometer on the Upper Atmosphere Research Satellite, Journal of Geophysical Research, 98, 10 725, doi:10.1029/93JD00227, 1993.

Sinnhuber, M., Nieder, H., and Wieters, N.: Energetic particle precipitation and the chemistry of the mesosphere/lower thermosphere, Surveys in Geophysics, 33, 1281–1334, 2012.

Siskind, D. E., Eckermann, S. D., McCormack, J. P., Coy, L., Hoppel, K. W., and Baker, N. L.: Case studies of the mesospheric response to recent minor, major, and extended stratospheric warmings, Journal of Geophysical Research Atmospheres, 115, 1–16, doi:10.1029/2010JD014114, 2010.

Skinner, W. and Hays, P.: Brightness of the O2 atmospheric bands in the daytime thermosphere, Planetary and Space Science, 33, 17–22, doi:10.1016/0032-0633(85)90138-2, 1985.

Slanger, T., Cosby, P., Sharpee, B., Minschwaner, K., and Siskind, D.: O ($1S \rightarrow 1D$, $3P$) branching ratio as measured in the terrestrial nightglow, Journal of Geophysical Research: Space Physics, 111, 2006.

Slanger, T. G. and Copeland, R. A.: Energetic Oxygen in the Upper Atmosphere and the Laboratory, Chemical Reviews, 103, 4731–4765, doi:10.1021/cr0205311, 2003.

Smith, A., Harvey, V., Mlynczak, M. G., Funke, B., García-Comas, M., Hervig, M., Kaufmann, M., Kyrölä, E., López-Puertas, M., McDade, I., et al.: Satellite observations of ozone in the upper mesosphere, Journal of Geophysical Research: Atmospheres, 118, 5803–5821, 2013.

Smith, I. W. M.: The role of electronically excited states in recombination reactions, International Journal of Chemical Kinetics, 16, 423–443, doi:10.1002/kin.550160411, 1984.

Stegman, J. and Murtagh, D.: The molecular oxygen band systems in the UV nightglow: measured and modelled, Planetary and Space Science, 39, 595–609, 1991.

Thomas, R. J., Barth, C. A., Rottman, G. J., Rusch, D. W., Mount, G. H., Lawrence, G. M., Sanders, R. W., Thomas, G. E., and Clemens, L. E.: Ozone density distribution in the mesosphere (50-90 km) measured by the SME limb scanning near infrared spectrometer, Geophysical Research Letters, 10, 245–248, doi:10.1029/GL010i004p00245, 1983.

Thomas, R. J., Barth, C. A., Rusch, D. W., and Sanders, R. W.: Solar Mesosphere Explorer Near-Infrared Spectrometer: Measurements of 1.27-μm radiances and the inference of mesospheric ozone, Journal of Geophysical Research: Atmospheres, 89, 9569–9580, 1984.

Wayne, R. P.: Singlet oxygen in the environmental sciences, Research on Chemical Intermediates, 20, 395–422, doi:10.1163/156856794X00397, 1994.

Winick, J., Wintersteiner, P., Picard, R., Esplin, D., Mlynczak, M., Russell, J., and Gordley, L.: OH layer characteristics during unusual boreal winters of 2004 and 2006, Journal of Geophysical Research: Space Physics, 114, 2009.

Wraight, P.: Association of atomic oxygen and airglow excitation mechanisms, Planetary and Space Science, 30, 251 – 259, doi:10.1016/0032-0633(82)90003-4, 1982.

Yamamoto, H., Makino, T., Sekiguchi, H., and Naito, I.: Infrared atmospheric band airglow radiometer on board the satellite OHZORA., Journal of geomagnetism and geoelectricity, 40, 321–333, 1988.